Publication Year	2021
Acceptance in OA@INAF	2022-06-07T13:31:46Z
Title	Study of the thermal and nonthermal emission components in M 31: the Sardinia Radio Telescope view at 6.6 GHz
Authors	Fatigoni, S.; Radiconi, F.; Battistelli, E. S.; MURGIA, MATTEO; CARRETTI, ETTORE; et al.
DOI	10.1051/0004-6361/202040011
Handle	http://hdl.handle.net/20.500.12386/32216
Journal	ASTRONOMY & ASTROPHYSICS
Number	651

A&A 651, A98 (2021)
https://doi.org/10.1051/0004-6361/202040011
© ESO 2021

Astronomy & Astrophysics

Study of the thermal and nonthermal emission components in M 31: the Sardinia Radio Telescope view at 6.6 GHz ⋆

S. Fatigoni[1,2], F. Radiconi[1,3], E. S. Battistelli[1,3,4], M. Murgia[4], E. Carretti[5], P. Castangia[4], R. Concu[4], P. de Bernardis[1,3], J. Fritz[6], R. Genova-Santos[7,8], F. Govoni[4], F. Guidi[7,8], L. Lamagna[1,3], S. Masi[1,3], A. Melis[4], R. Paladini[9], F. M. Perez-Toledo[8], F. Piacentini[1,3], S. Poppi[4], R. Rebolo[7,8], J. A. Rubino-Martin[7,8], G. Surcis[4], A. Tarchi[4], and V. Vacca[4]

[1] Sapienza University of Rome, Physics Department, Piazzale Aldo Moro 5, 00185 Rome, Italy
e-mail: federico.radiconi@roma1.infn.it, elia.battistelli@roma1.infn.it
[2] University of British Columbia, Department of Physics and Astronomy, Vancouver, BC V6T 1Z1, Canada
e-mail: sfatigoni@phas.ubc.ca
[3] INFN Sezione di Roma, Piazzale Aldo Moro 5, 00185 Rome, Italy
[4] INAF Osservatorio Astronomico di Cagliari, Via della Scienza 5, 09047 Selargius, CA, Italy
[5] INAF Istituto di Radioastronomia, Via P. Gobetti 101, 40129 Bologna, Italy
[6] Instituto de Radioastronomia y Astro sica, UNAM, Campus Morelia, A.P. 3-72, CP 58089, Mexico
[7] Instituto de Astro sica de Canarias, Vía Lactea s/n, 38205 La Laguna, Tenerife, Spain
[8] Departamento de Astrofísica, Universidad de La Laguna (ULL), 38206 La Laguna, Tenerife, Spain
[9] Infrared Processing Analysis Center, California Institute of Technology, Pasadena, CA 91125, USA

Received 27 November 2020 / Accepted 20 April 2021

ABSTRACT

Context. The Andromeda galaxy is the best-known large galaxy besides our own Milky Way. Several images and studies exist at all wavelengths from radio to hard X-ray. Nevertheless, only a few observations are available in the microwave range where its average radio emission reaches the minimum.
Aims. In this paper, we want to study the radio morphology of the galaxy, decouple thermal from nonthermal emission, and extract the star formation rate. We also aim to derive a complete catalog of radio sources for the mapped patch of sky.
Methods. We observed the Andromeda galaxy with the Sardinia Radio Telescope at 6.6 GHz with very high sensitivity and angular resolution, and an unprecedented sky coverage.
Results. Using new 6.6 GHz data and Effelsberg radio telescope ancillary data, we confirm that, globally, the spectral index is 0.7 ± 0.8, while in the star forming regions it decreases to 0.5. By disentangling (gas) thermal and nonthermal emission, we find that at 6.6 GHz, thermal emission follows the distribution of HII regions around the ring. Nonthermal emission within the ring appears smoother and more uniform than thermal emission because of diffusion of the cosmic ray electrons away from their birth-places. This causes the magnetic fields to appear almost constant in intensity. Furthermore, we calculated a map of the star formation rate based on the map of thermal emission. Integrating within a radius of $R_{max} = 15$ kpc, we obtained a total star formation rate of $0.19 \pm 0.01\ M_\odot\ yr^{-1}$ in agreement with previous results in the literature. Finally, we correlated our radio data with infrared images of the Andromeda galaxy. We find an unexpectedly high correlation between nonthermal and mid-infrared data in the central region, with a correlation parameter $r = 0.93$. Finally, by computing the logarithmic 24 μm–21 cm ratio $q_{24\ \mu m}$, we find a decreasing trend with increasing galactocentric distance and an increasing dispersion. The logarithmic far-infrared-to-radio ratio is found to be $q_{FIR} = 2.41 \pm 0.04$.

Key words. galaxies: individual: Messier 31 — radio continuum: galaxies — ISM: general — radiation mechanisms: non-thermal — radiation mechanisms: thermal

1. Introduction

The Andromeda galaxy (Messier 31, M 31) is the largest galaxy of the Local Group, which includes the Milky Way, the Triangulum galaxy (M 33), and several other smaller galaxies including the satellite Messier 32 (M 32) and Messier 110 (M 110). Messier 31 is a large disk galaxy at a distance of 780 kpc from Earth (Stanek & Garnavich 1998), and has a proper redshift of $z = -0.001$ (de Vaucouleurs et al. 1991), where the negative value shows that it is moving towards the Milky Way.

The galaxy presents a large central bulge. The bulge is defined as the central region that has an extension of $0.5°$ in the optical band, corresponding to a proper size of 1.1 kpc (Morton et al. 1977). The bulge contains dilute ionized gas and a few dense star clusters. V- and I-band Hubble Space Telescope (HST) Planetary Camera images show that the central region seems to have two separate concentrations of light that are about $0.5''$ apart (Lauer et al. 1993). One of these probably contains a dense central object, presumably a black hole of mass $M_{BH} \sim 10^8\ M_\odot$, while the other might be a star cluster. There is a ring circling the bulge at a radius of about 10 kpc, and most of the young disk stars lie in this ring or just outside it (Haas et al. 1998; Gordon et al. 2006; Ford et al. 2013). Going to greater distances from the center we find the HI (Braun et al. 2009) layer that flares out to become thicker. The M 31 galaxy is the brightest of the Messier objects, with an apparent magnitude of $V = 3.4$ (Gil de Paz et al. 2007) and an apparent extension of approximately $1.3\ deg^2$ (Nilson 1973) due to the high inclination with respect

⋆ Table A.1 and the 6.6 GHz SRT map are only available at the CDS via anonymous ftp to cdsarc.u-strasbg.fr (130.79.128.5) or via http://cdsarc.u-strasbg.fr/viz-bin/cat/J/A+A/651/A98

to the line of sight, which is assumed to be of 77° (Gordon et al. 2006) considering that 90° means an edge-on orientation.

Observations by the infrared Spitzer Space Telescope revealed that M 31 contains about 10^{12} stars (Peñarrubia et al. 2014), which is at least twice the number of stars contained in the Milky Way, and the total mass of the galaxy is estimated to be $M_{M\,31} = 1.5 \times 10^{12}\ M_\odot$ (Barmby et al. 2006). High-resolution (FWHM = 9″) Westerbork Synthesis Radio Telescope (WSRT) observations of the 21 cm line by Braun et al. (2009) were used to calculate the total neutral gas mass, which turned out to be in the range 4.4 to $5 \times 10^9\ M_\odot$ (Fritz et al. 2012). CO observations by Nieten et al. (2006) within a field of 5×1.8 led to an estimate of the mass of molecular gas of the order of $6.2 \times 10^8\ M_\odot$ (Fritz et al. 2012). While the former observations do not include the whole galaxy disk, they most certainly encompass the majority of the molecular gas (about 95% of the total molecular mass, according to Nieten et al. 2006).

Because of its size and distance in the sky, M 31 is an excellent laboratory with which to further study and perhaps confirm the physical mechanisms and properties that have so far only been studied in detail in our own Galaxy. It also provides information about the general features of a typical disk galaxy. The M 31 galaxy has been studied at several wavelengths. The Fermi-LAT was used to detect γ-ray emission in the energy range 200 MeV – 20 GeV (Abdo et al. 2010). NuSTAR permitted the study of hard X-ray emission allowing X-ray binaries and neutron stars/black holes to be resolved (Wik et al. 2016). XMM, ROSAT, and Chandra were used to study its X-ray emission (Stiele et al. 2010). Ultraviolet (UV) measurements were used to study interstellar extinction (Clayton et al. 2015) as well as the circumgalactic medium, finding a very extended ionized medium which may overlap with a similar one originating from our Milky Way (Lehner et al. 2020). Optical and near-infrared (NIR) observations were used to investigate the stellar composition (Sick et al. 2014). The IR and submillimeter (submm) emission of M 31 were studied by Fritz et al. (2012) and the HELGA collaboration. These latter authors used data obtained from the Herschel satellite to characterize the dust emission of M 31, and to construct maps of the dust surface density, the dust-to-gas ratio, the starlight heating intensity, and the abundance of polycyclic aromatic hydrocarbons (PAHs).

The radio and microwave emission of M 31 have been observed at high angular resolution (FWHM < 5′) in the last three decades with the Effelsberg radio telescope (Beck et al. 2020; Berkhuijsen et al. 2003, 1983), the Westerbork Synthesis Radio Telescope (WSRT, Braun et al. 2009), and the Very Large Array (VLA, Condon et al. 1998). Combined Effelsberg and VLA observations at 1.46 GHz and Effelsberg data at 4.85 GHz indicate a global nonthermal spectral index of $_s = 1.0 \pm 0.1$ (Berkhuijsen et al. 2003), which is consistent with the value found by Battistelli et al. (2019), who studied the overall flux density emission from radio to IR wavelengths. Berkhuijsen et al. (2003), assuming a nonthermal spectral index equal to 1, derived (gas-) thermal and nonthermal maps at 4.85 GHz, finding that the thermal emission is stronger in the northern part of M 31, whereas the nonthermal emission is nearly homogeneous over the whole ring. This homogeneity suggests that recent star formation does not lead to a local increase in the number of relativistic electrons and magnetic field strength. Strong thermal emission was also found within the central region of the galaxy. Beck et al. (2020) used three new deep radio surveys of M 31 made with the Effelsberg radio telescope at 2.645 GHz, 4.85 GHz, and 8.35 GHz to perform a detailed study of the spectral index maps as well as thermal and nonthermal emission scale lengths. Beck et al. (2020), using nine frequencies, found a total spectral index of -1.10 ± 0.02 and a synchrotron spectral index of -1.31 ± 0.03; they also found that the synchrotron emission ring is wider than the thermal emission one.

In Battistelli et al. (2019) we showed that the total integrated emission at 6.6 GHz from M 31, integrated over an elliptical region of 9.15° and 5.95° semi-axes, is at the level of 1.20 ± 0.06 Jy. Comparing different ancillary data allowed us to calculate the emission budget; we found strong and highly significant evidence for anomalous microwave emission (AME) at the level of $1.45^{+0.17}_{-0.19}$ Jy at the peaking frequency of 25 GHz. By decomposing the spectrum into known emission mechanisms, such as synchrotron, free-free, thermal dust, and AME, we found that the overall emission from M 31, at frequencies below 10 GHz, is dominated by synchrotron emission with a spectral index of $-1.10^{+0.10}_{-0.08}$, with subdominant free-free emission. At frequencies of 10 GHz, AME has a similar intensity to that of synchrotron and free-free emission, overtaking these components at frequencies between 20 GHz and 50 GHz, whereas thermal dust emission dominates the emission budget at frequencies above 60 GHz, as expected. For the purpose of this paper, we refer to the free-free emission as thermal emission, and to the synchrotron emission as nonthermal emission, assuming any other emission mechanism to be negligible at 6.6 GHz. K-band observations with improved angular resolution (e.g., 9′ with the Sardinia Radio Telescope at 22 GHz) will be key to disentangling AME models, and to studying AME over an entire galaxy outside of our own with high angular resolution (Battistelli et al. 2012; Radiconi et al., in prep.).

This paper is organized as follows. The characteristics of the observations, the scanning strategy, and the data analysis pipeline of C-band data are described in Sect. 2. In Sect. 3 we describe all the ancillary maps used in this paper and the recipes that were adopted to make their geometry and angular resolution uniform. The removal of compact sources is presented in Sect. 4. In the same section we also compare the normalized differential count of compact sources with theoretical predictions. In Sect. 5 we carry out an analysis of the morphology of M 31 by investigating the galaxy spectral index map. Thermal and nonthermal maps at 6.6 GHz are presented in Sect. 6, while in Sect. 7, starting from the thermal map, we derive a map of the star formation rate (SFR), and compare this to what was previously found in the literature. In Sects. 8 and 9 we analyze the correlation between radio-continuum and IR data, studying how thermal and nonthermal emissions are related to IR emission. We also compute the parameter q_{FIR} and compare the result with the expected value. Finally, in Sect. 10 we summarize our results.

2. Sardinia Radio Telescope observations of M 31

2.1. Sardinia Radio Telescope

The Sardinia Radio Telescope (SRT[1]) is an Italian facility for radio astronomy run by the Istituto Nazionale di Astrofisica, INAF, which was formally inaugurated in 2013 after completion of technical commissioning (Bolli et al. 2015). The scientific commissioning of the telescope was carried out in the period 2012–2015 (Murgia et al. 2016; Prandoni et al. 2017). At the beginning of 2016 the first call for single-dish early science programs (ESPs) was issued, and the observations started on February 1, 2016. The SRT observations of M 31 at 6.6 GHz presented in this work are part of these ESPs. The SRT is placed

[1] http://www.srt.inaf.it/

35 km north of Cagliari (Lat: 39°29′34″N Long: 9° 14′42″E) on the island of Sardinia at 600 m above sea level. The optical system is based on a quasi-Gregorian dish antenna, with a primary mirror of 64 m in diameter, and a secondary mirror of 9 m, which is shaped in such a way as to minimize the standing wave bouncing between the two reflectors. Three additional mirrors increase the number of focal positions. A key feature of the SRT is its active surface, composed of a total of 1116 electromechanical actuators able to correct deformations induced by gravity on the primary surface. The SRT has an angular resolution of 2.9′ (FWHM) at a frequency of 6.6 GHz.

The suite of backends currently available on site includes SARDARA (SArdinia Roach2-based Digital Architecture for Radio Astronomy; Melis et al. 2018). The SARDARA backend is a wide-band digital backend based on ROACH2[2] technology, and can divide the signal in the given bandwidth into up to 16 384 channels for spectropolarimetric observations. We used this backend for our observations.

2.2. C-band observation

The main goal of the observations presented in this paper is to map the whole M 31 galaxy in the C-band down to a sensitivity of 0.4 mJy beam^{-1} in order to create a high-sensitivity, high-angular-resolution map of M 31 microwave emission covering its full extension, limited by the confusion noise at this frequency and angular resolution (Bondi et al. 2003; Condon 1974). We set the Local Oscillator at 5.9 GHz and we use the SARDARA configuration with 1.5 GHz bandwidth sampled with 16 384 channels of 91.6 kHz in width. The data cube will be analyzed in greater detail in a search for spectral line emission from various transitions (Tarchi et al., in prep.). We set the Focus Selector filter to select the frequency range from 6.0 to 7.2 GHz, which defines our observing bandwidth. The central frequency of our observations is therefore 6.6 GHz. Traditionally, C-band is centered at about 5 GHz, while the band around 6.6 GHz is known as the C-high band. For simplicity, in this paper we refer to the 6.6 GHz data as C-band data.

We decided to cover the galaxy with a rectangle of 7.4 deg^2 centered at (RA; Dec) = ($0^h42^m48^s$; +41 16′48″). To the best of our knowledge, this is the biggest map ever produced at this frequency and angular resolution with a single-dish radio telescope.

The map size was determined by the minimum contour that includes the galaxy, to which we added a Map Edge of 0.25 deg in each of the two scanning directions. The minimum contour was estimated by comparing the two maps provided by Herschel/SPIRE at 250 μm (Fritz et al. 2012) and Planck at 857 GHz (Planck Collaboration VI 2014); which are supposed to trace the galaxy in its maximum extension. The aim of adding an extra padding is to have a sky region that is completely free from M 31 emission and that we can use to estimate the background and decouple this from the signal coming from the galaxy. We adopted an on-the-fly map-scanning strategy, which means orthogonal subscans along right ascension (RA) and declination (Dec) spaced by 54 arcsec (FWHM/3). We used a scanning speed of 6′ s^{-1}. Covering the 7.4 deg^2 of our map required 209 RA subscans and 161 Dec subscans. Table 1 reports the main details of the observations.

Before starting the observations, a set of daily preliminary operations were performed. These include the configuration of the backend, setting of the amplifier attenuation factors (to ensure linearity), secondary mirror positioning (by focusing a bright radio source), and spectroscopic system acquisition and pointing checks. The calibrators were observed during each session, when M 31 was over the antenna critical elevation of 85 deg, the SRT being equipped with an Alt-azimuthal mount. The observations were completed in 64 h, divided in 6 days, during which we carried out 22 complete scans of the galaxy.

Table 1. Main characteristics of the C-band SRT observations on M 31.

Telescope	SRT (64 m)
Receiver	C-band (5.7–7.7 GHz)
Backend	SARDARA
Spectroscopy	16 384 channels
Backend bandwidth	1.5 GHz
Channel spacing	91.6 kHz
Observed frequency range	6.7–7.025 MHz
Beam size	2.9′ at 6.6 GHz
Polarization	Full stokes
Scanning strategy	Orthogonal raster subscans
Scanning speed	6′ s^{-1}
Sample rate	25 spectra s^{-1}
$\langle T_{sys} \rangle$	37 K
Map size	2.4 deg × 3.1 deg ≃ 7.4 deg^2
Total number of scans	22 RA + 22 Dec
Total observation time	64 h
Reached sensitivity	0.43 mJy beam^{-1}

2.3. Data acquisition

Once collected, the data were analyzed using the Single-dish Spectral-polarimetry Software (SCUBE, see Murgia et al. 2016), which was created specifically for treating data acquired with the SRT. SCUBE is a package dedicated to the reduction and analysis of single-dish data and its combination with interferometric observations. SCUBE is written in C++ and is developed and maintained by M. Murgia and F. Govoni; it allowed us to import the data, extract, analyze, and flag the spectra, do the baseline subtraction, perform calibration, and generate the final maps with different methods.

As a first step in the data reduction process we removed the backend birdies (dead channels occurring in SARDARA data) and the well-known persistent radio-frequency interference (RFI) that affect specific spectral windows at the SRT. These omnipresent signals were removed a priori by applying the same flag table to all observing days. All the remaining sporadic RFI signals (e.g. satellites or other transient ambience disturbances) were removed later in the analysis with automated flagging methods. Overall, the amount of data erased due to RFI accounts for about 30% of the total.

The baseline subtraction was carried out differently for the calibrators and for the M 31 scans. To estimate the baseline for calibrators we made a linear fit over 10% at the beginning and at the end of each subscan, and then removed this linear trend from the data.

To create a baseline model for the M 31 scans we used a mask to cover the part of the map that we knew could possibly contain either galactic emission from M 31 itself or any bright background point source. The remaining part of the field of view was considered as "cold sky" and was used to perform a linear fit to the baseline subscan by subscan (see Sect. 2.5).

[2] https://casper.ssl.berkeley.edu/wiki/ROACH2

2.4. Calibration

Data calibration included bandpass and flux density calibration. These were carried out at the beginning of the map extraction process and performed channel by channel. The bandpass calibration was necessary to set the instrument responsivity for every channel. For this purpose we used specific calibrators, like J0542+4951 (3C147), with stable and known spectra.

We applied the gain-elevation curve correction to account for the gain variation with elevation due to the gravitational stress changes in the telescope structure. We do not compensate for the atmosphere opacity however, considering that the correction is negligible at these frequencies.

The counts-to-Jansky conversion factor was derived by means of a two-dimensional Gaussian fit to the Stokes I and R images of the standard flux density calibrators 3C147, J0137+3309 (3C48), J1331+3030 (3C286), and J1445+1212 (3C295). We adopted the flux density scale of Perley & Butler (2013). The systematic uncertainty is assumed to be 5% of the calibrator flux density.

All calibrator observations were made during the interruption of the M 31 scans when the galaxy was too highly elevated on the sky or at the end of the scans. Data were acquired during four cross scans on each of the calibration sources. The cross scans were made at a velocity of 1^{0}s^{-1} and each subscan was 20^{0} long.

2.5. Baseline subtraction

Before stacking the subscans to form the maps, we performed a subscan baseline removal in order to set all the emission coming from blank fields to zero. To this purpose we applied a mask. Our mask map was created starting from three different maps of the M 31 region: the NRAO VLA Sky Survey (NVSS) map at 1.4 GHz (Condon et al. 1998) which contains point sources, the Spitzer MIPS map at 12.5 THz (Gordon et al. 2006), and the Planck 850 GHz map (Planck Collaboration I 2020) that traces the extension of the galaxy with thermal dust emission. We renormalized and combined the set of maps creating a mask from which the baseline is calculated. The mask, combined with the 0.25 deg MapEdge, was finally used to estimate the background level by fitting a linear model to the emission in the non-masked region.

At this point, in order to generate the final map, we performed a new flagging of the data to remove isolated spikes or short-time RFIs in an automated fashion. Following this approach, we were able to flag all the data that deviate by more than 3 , where is a combination between the single subscan rms and the sky model noise according to:

$$^{2} = \mathrm{rms}^{2}_{\mathrm{sub\ scan}} + \mathrm{mod_errsys}\,\mathrm{model}^{2} : \quad (1)$$

The parameter mod_errsys was chosen to be 0.5. This method was iterated until convergence was reached: three iterations for each set of data were needed. At this point, it was possible to create a new set of images where, as expected, the rms level was lower with respect to the previous images.

2.6. Map making

In the creation of our final total intensity map, we combined the scans by taking an average of all of them in order to increase the signal-to-noise ratio. A direct stacking would be heavily affected by the scanning noise present in the individual on-the-fly maps, which takes the form of the typical pattern of stripes oriented along the scanning direction. These stripes can be due to imperfect RFI removal or short-term fluctuations in the atmosphere or in the receiver gain. Sometimes these features are not totally removed during the flagging and the baseline subtraction process, and so they persist in the final map. These features are easier to identify if we analyze the map in the perpendicular direction with respect to the direction of the corrupted subscan (Emerson & Graeve 1988). To this purpose, SCUBE implements both Fourier and wavelet map-making methods. In the Fourier transform plane, the scanning noise terms from any single scan appear only on a narrow band passing through the origin, with a width inversely proportional to the characteristic scale lengths of the baseline drifts in the original scan. The final map is created by incorporating a second scan in an orthogonal direction so that once the second scan is also transformed in the Fourier plane, the second map only intersects the error terms of the first map at the origin. The knowledge of the approximate scale length of the baseline drift of each map, and so the width of each band error in the Fourier plane, enables an optimally weighted combination of Fourier terms of each data set to be made (Emerson & Graeve 1988). In the wavelet space, the logic is the same, except that the unwanted scanning noise is isolated and filtered out using a convenient merging of the stationary wavelet transform (SWT) coefficients (Murgia et al. 2016). One advantage of the SWT method compared to the Fourier method is that there is no need to determine an optimal width for the weights of the noise bands. While the noise bands partially overlap at the center of the Fourier plane, they are completely separated in the wavelet domain. Indeed, the horizontal and vertical detail coefficients of the two orthogonal scans can be opportunely mixed while the diagonal detail coefficients and the approximation coefficients are averaged.

We verified that both the Fourier and SWT de-stripping techniques give consistent results. However, we noted that the SWT performed slightly better than the Fourier method and therefore we opted the former.

As a last step in the map-making process we corrected the final map for the residual base level. To this purpose, we masked the emission from M 31 and applied the Papoulis-Gerchberg Algorithm (PGA, Papoulis 1975) to model and interpolate the surrounding base level over the excluded data. SCUBE provides an application of the PGA that allows the user to reconstruct the missing part of an image by imposing a low pass filter in the spectral domain. The signal extrapolation is carried out by iterating alternately between time (spatial) and spectral domains until convergence is reached. To this end, we masked out an elliptical region of $9^{\circ}.5$ and $5^{\circ}.5$ semi-major and semi-minor axis, respectively (PA = 52 deg), centered on the innermost regions, and we reconstructed the missing signal by imposing that the reconstructed map retains no power below a spatial scale corresponding to the ellipse major axis. This is achieved by a convolution with a Gaussian tapering in the spectral domain. The reconstructed base-level image is then subtracted from the final map, which allows the removal of residual large-scale features left over after baseline removal and map-making, and large-scale features in foreground and background emission, bringing the map back to a zero-level outside the galaxy, as already shown in Battistelli et al. (2019). Figure 1 shows our final map of M 31 at 6.6 GHz.

2.7. Map statistics

In order to provide an estimate of the sensitivity level reached in our map, we masked the emission from point-like radio

sources. Details on how compact sources are removed from the map are reported in Sect. 4. In our source-subtracted map, considering our pixel size of $3'.9$, and the SRT beam in the C-band, we derived the rms fluctuations from two 0.4 deg^2 uncontaminated regions. We repeated the same analysis on the SWT map before and after applying the flagging. We found consistent (although slightly different) results in the two maps: we obtained a rms mean value of 0.44 mJy beam^{-1} before flagging and 0.43 mJy beam^{-1} after flagging. Therefore, from this first analysis, we have a final value for the rms of 0.43 mJy beam^{-1}. This value is fully compatible with the expected value from confusion noise, assuming a spectral index of 0.7: $\sigma_{confnoise} = 0.44$ mJy beam^{-1} (Condon 1974).

3. Ancillary data

In this section we describe the ancillary maps used throughout this work. The ancillary maps are described in two different sections, one relative to radio and microwave wavelengths and the other to IR observations.

3.1. Radio data

For radio wavelengths, we used three maps acquired with the Effelsberg Radio Telescope[3], at 1.46 GHz, 2.7 GHz, and 4.85 GHz. With its 100-m primary mirror diameter, Effelsberg reaches an angular resolution of $9'.5$ (Beck & Grave 1982) and $2'.8$ (Berkhuijsen et al. 2003) at 2.7 GHz and 4.85 GHz, respectively. The 1.46 GHz map angular resolution of $9'.5$ (Beck et al. 1998) was achieved combining Effelsberg data with VLA data. Moreover, we used the SRT map at 1.385 GHz (Melis et al. 2018), with an angular resolution of $9'.3$, to correlate radio and IR data.

3.2. Infrared data

Infrared data were used to characterize stellar and dust emission and explore the presence of possible correlations with the radio continuum emission (see Sect. 8). For this purpose, we used the Spitzer Space Telescope[4]-[5] maps at 24 μm and 3.6 μm. These two maps were chosen for correlation purposes because the 24 μm (Gordon et al. 2006) map is a SFR tracer, while the 3.6 μm (Barmby et al. 2006) is a tracer of older stars. The angular resolution of the Spitzer 24 μm map is $6'.0$, while the 3.6 μm map is characterized by a resolution of $1'.9$.

In order to estimate the radio/IR ratio, q_{FIR}, following the convention by Helou et al. (1985), we also used the IRAS 60 μm map (Xu & Helou 1996) and the Herschel 100 μm map (Fritz et al. 2012). The angular resolutions of the two maps are $4'.0$ and $9'.5$, respectively.

3.3. Ancillary data treatment

Each one of the aforementioned maps is characterized by a given angular resolution and geometry (i.e., pixelization on the sky). In order to compare different maps, it was necessary to bring all of them to the same coordinate system and angular resolution.

We used the Montage 6.0 software[6] to modify the coordinate system of the maps and convert it to the SRT C-band pixelization. Once all the maps were in the same World Coordinate System (WCS, Mink 1997) reference frame, they were convolved to the same angular resolution.

Depending on the purpose, three different final angular resolutions were used: $14'.5$, $10'.0$, and $3'.0$.

For the sole purpose of estimating the q_{FIR} parameter, the Herschel 100 μm map and the IRAS 60 μm map were convolved to the common resolution of $14'$.

Convolution of all the maps to the resolution of the Effelsberg 2.7 GHz map ($9'.5$) was carried out to disentangle thermal and nonthermal emission (see Sect. 6) and to correlate these two emission mechanisms to IR data (see Sect. 8).

We convolved the two Spitzer maps, the 1.4 GHz Effelsberg, and our SRT C-band image to $9'.3$ to extract a spectral index map (see Sect. 5).

4. Compact sources

A large number of sources can be seen in the 4.23.1 deg^2 C-band map shown in the left panel of Fig. 1. In order to calculate a proper estimate of the intrinsic brightness of M 31, it is necessary to identify and remove all the signals coming from these sources. To this end, we generated a point-source catalog of M 31 at 6.6 GHz. Aside from point-source subtraction, we used this catalog to verify the theoretical prediction on the number of sources we expect to find with a certain flux density in a given area, according to a specific model.

We started by extracting a point-source catalog from the NRAO VLA Sky Survey at 1.4 GHz (Condon et al. 1998) which has an angular resolution of $45''$ and a rms of 0.5 mJy beam^{-1}. We relied on the relatively high angular resolution and sensitivity of the NVSS to obtain a good prior for the coordinates of the points sources in the direction of the M 31 field. This is particularly helpful in the subtraction of those point sources seen in projection against (or embedded in) the extended emission of the galaxy, as we show in Fig. 2 where the SRT C-band contours are added to the NVSS image. Indeed, the finer NVSS resolution also allowed us to resolve nearby sources not easily discernible from our single-dish resolution. We note that we excluded the M 31 central region extended emission from the NVSS image in the point-source subtraction process.

We select in the NVSS map all the point sources with a peak flux density of $F > 5$ mJy at 1.4 GHz. By fitting these point sources with a 2D Gaussian, we compiled a catalog that contains the peak flux densities and the coordinates for a large number of sources both inside and in the immediate surroundings of the M 31 field.

In order to account for nonzero offset over which the source may lie, we added to the Gaussian model a plane with an offset and a tilt as free parameters. This made the fit more accurate for sources with a significant local base level, in particular those seen in projection over the M 31 emission. As a further step, the NVSS catalog coordinates were used as input parameters in the CATS[7] (Verkhodanov et al. 1997) database in order to extract the radio flux density information available in the literature about these sources at other frequencies in the radio band. We then extracted the flux densities of the point sources present in the 6.6 GHz SRT image using as a prior the coordinates of the NVSS catalog. By fitting the same 2D Gaussian + base level model over each one of the NVSS coordinates pairs we obtained the peak flux density at 6.6 GHz. The fit was performed only if the SRT peak in the NVSS position is $> 3\sigma$, where σ is the noise

[3] https://www.mpifr-bonn.mpg.de/en/effelsberg
[4] https://www.mpifr-bonn.mpg.de/3265873/m31
[5] http://www.spitzer.caltech.edu/
[6] http://montage.ipac.caltech.edu/
[7] www.sao.ru/cats/

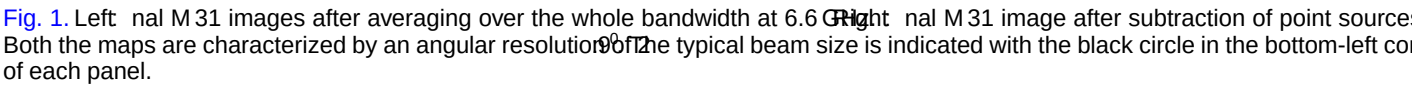

Fig. 1. Left nal M 31 images after averaging over the whole bandwidth at 6.6 GHz. Right nal M 31 image after subtraction of point sources. Both the maps are characterized by an angular resolution of 9.0 FWHM. The typical beam size is indicated with the black circle in the bottom-left corner of each panel.

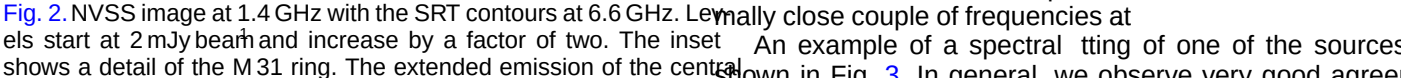

Fig. 2. NVSS image at 1.4 GHz with the SRT contours at 6.6 GHz. Levels start at 2 mJy beam^{-1} and increase by a factor of two. The inset shows a detail of the M 31 ring. The extended emission of the central region (grey area) has been excluded from the point-source search.

of the map, or 1.6 mJy beam^{-1} pixel^{-1} for the SRT C-band map. Out of the all the sources present in the initial NVSS catalog, we detected 93 counterparts at 6.6 GHz inside the eld of the C-band SRT map broadly delimited by the black contours in Fig. 2.

Finally, we merged the CATS catalog with the SRT C-band catalog leading to a nal list of point sources containing both the source positions and all the spectral information available in the literature for these objects. The radio spectra of all these compact sources were modeled with a modi ed power:

$$\log(F) = \log\left(\frac{}{\text{ref}}\right) + \log(A) + k\left(e^{\log\frac{}{\text{ref}}}\right); \quad (2)$$

where k is a curvature term, A is the amplitude at the reference frequency $_{\text{ref}}$, and is the spectral index of the unmodi ed power law. The model converges to the usual power law with index in the limit $k \to 0$. We adopted for reference frequency the xed value $_{\text{ref}} = 1$ GHz. The observed radio spectra were t-ted with the modi ed power law model when at least three data points were available, otherwise we xed the curvature to $k = 0$, resorting to an ordinary power law.

For signi cantly curved spectra, only the spectral index between a very close couple of frequencies is meaningful. Nonetheless, a local spectral index value at a given frequency, , can be easily computed di erentiating Eq. (2) with respect to $\log\frac{}{\text{ref}}$:

$$= k\log\left(\frac{}{\text{ref}}\right)\left(e^{\log\frac{}{\text{ref}}}\right): \quad (3)$$

This can be viewed as the spectral index between an in nitesimally close couple of frequencies at .

An example of a spectral tting of one of the sources is shown in Fig. 3. In general, we observe very good agreement between the SRT ux densities and the measurements from the literature. Moreover, in Fig. 3 we show that in the case of this bright source there is also evidence that the SRT in-band spectral index measured at four distinct frequencies between 6.0 and 7.2 GHz is consistent with the trend of both the model t and the measurements at nearby frequencies taken from the literature.

The image of the SRT point-source model at 6.6 GHz is shown in Fig. 4 at an angular resolution of 2.9 FWHM. We recall that the SRT at C-band point-source model is a subset of the larger initial catalog based on the NVSS which comprises a larger eld in the sky. Indeed, by using the NVSS-based coordinates and the best- t parameters of the modi ed power law in Eq. (2), it is in principle possible to generate a point-source model image at any desired frequency and angular resolution. Moreover, this procedure was followed to remove the point-source contribution from

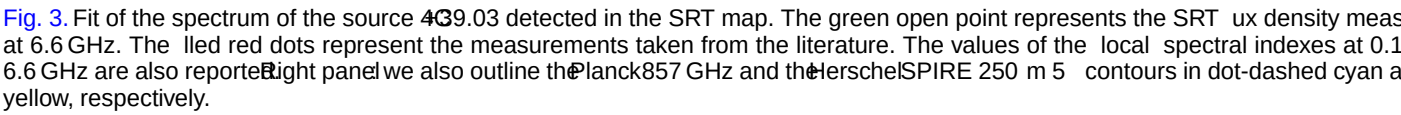

Fig. 3. Fit of the spectrum of the source 4C39.03 detected in the SRT map. The green open point represents the SRT flux density measurement at 6.6 GHz. The filled red dots represent the measurements taken from the literature. The values of the local spectral indexes at 0.15, 1.4, and 6.6 GHz are also reported. Right panel: we also outline the Planck 857 GHz and the Herschel SPIRE 250 μm 5σ contours in dot-dashed cyan and yellow, respectively.

Fig. 4. SRT C-band point-source model.

the global M 31 spectral energy distribution (SED) in Battistelli et al. (2019).

A catalog of all the compact radio sources in the SRT map and the best-fit parameters are reported in Table A.1, while in Fig. A.1 we show all the 93 fits of the spectra. Table A.1 also reports the spectral indexes measured between 1.4 and 6.6 GHz, $\alpha^{6.6\,\mathrm{GHz}}_{1.4\,\mathrm{GHz}}$. The data at 1.4 GHz refer to the NVSS catalog.

4.1. Spectral index distribution

After obtaining the spectral index $\alpha^{6.6\,\mathrm{GHz}}_{1.4\,\mathrm{GHz}}$ for each source detected in C-band, it is possible to study the spectral index distribution, which is shown in Fig. 5. The average spectral index value is 0.72, while the median value is 0.81. The spectral index bin with most occurrences is 0.85 ± 0.95.

As expected, in most cases, the spectral index exhibits a positive value. Only 2 out of the 93 sources exhibit a negative spectral index, or equivalently an inverted spectrum. Approximately 74% of the sources exhibit a spectral index of $\alpha \geq 0.5$, indicating that their emission is most likely optically thin nonthermal synchrotron emission. This population is typically composed of background sources and supernova remnants (SNRs) in the M 31 field, as has been shown by Galvin & Filipovic (2014) and Lee & Lee (2014).

4.2. Differential source counts

Given the C-band flux densities for each of the 93 sources, the differential source counts were computed by binning the 0.007–0.45 Jy flux density range according to the values reported in Table 2. It is possible to compare the source counts with a theoretical model: here we use the latest version of the 4.8 GHz model[8] by Bonato et al. (2017). As our measurements were performed at 6.6 GHz, we extrapolated them to 4.8 GHz flux density for each source, according to:

$$F_{4.8\,\mathrm{GHz}} = F_{6.6\,\mathrm{GHz}} \left(\frac{6.6}{4.8}\right)^{\alpha^{6.6\,\mathrm{GHz}}_{1.4\,\mathrm{GHz}}}; \quad (4)$$

where $\alpha^{6.6\,\mathrm{GHz}}_{1.4\,\mathrm{GHz}}$ is the source spectral index; see Table A.1.

The choice of 0.007 Jy as the lower value to study the differential source counts can be justified assuming a Gaussian distribution, an rms value of 1.6 mJy pixel^{-1} within the C-band map extrapolated to 4.8 GHz, and a 3σ peak cut-off. We find that the sources with flux density of 0.007 Jy are detected with

[8] http://w1.ira.inaf.it/rstools/srccnt/

Fig. 5. Spectral index distribution between 1.4 and 6.6 GHz for the 93 detected point sources in the field of M 31.

Table 2. Number of sources detected in C-band map in a given flux density bin.

Range (Jy)	Count	$\log_{10}$ (Diff. count)	Theor. count
0.007 – 0.01	22	6.54	21
0.01 – 0.0135	16	6.33	14
0.0135 – 0.02	15	6.03	14
0.02 – 0.05	14	5.34	18
0.05 – 0.15	5	4.37	7
0.015 – 0.45	3	3.67	2

Notes. In the last column we show the number of expected sources in each bin from the model we are considering.

a probability of greater than 95%. It is important to stress that a non-negligible fraction (19%) of the detected sources have extrapolated flux densities at 4.8 GHz lower than 0.007 Jy; we do not make use of these.

Before comparing the measurements extrapolated to 4.8 GHz with the source-count model, the source counts $n(S)$ derived from the SRT flux densities were fitted with a power law $n(F) = A \left(\frac{F}{\mathrm{Jy}}\right)^{\gamma}$, where both the number density of sources per flux density interval at 1 Jy A and the spectral index γ are free parameters. The result of the fit in logarithmic scale is:

$$\frac{dN}{dF} = (300 \pm 80) \left(\frac{F}{\mathrm{Jy}}\right)^{-1.98 \pm 0.07} \mathrm{Jy}^{-1}\,\mathrm{sr}^{-1}. \quad (5)$$

The differential source counts and the best-fit curve are shown in Fig. 6. The horizontal error bars represent the bin widths, while the vertical ones correspond to the Poisson errors associated with the measurements.

At this point we can compare our source sample with the model from Bonato et al. (2017). This theoretical model returns the predicted Euclidean normalized differential radio source counts per steradian for a discrete series of flux densities. The Euclidean normalized differential counts is defined as $S^{2.5}\frac{dN}{dF}$, where F is in Jy. In Fig. 7, our source sample is compared with the 4.8 GHz model taking into account the 7 deg^2 observed area. The data are in good agreement with the model for the low-, intermediate-, and high-density values. The tension in the last point in Fig. 7 can be solved by removing from the counts the BLAZAR B3 0035+413 that at 4.8 GHz has an extrapolated flux density of 0.44 Jy.

Fig. 6. Point-source differential source counts and the fitted power law in double log scale. The error bars parallel to the flux density axis indicate the bin widths.

Fig. 7. Normalized differential point-source counts compared with the Bonato et al. (2017) model at 4.8 GHz.

Integrating the model from 0.007 to 0.45 Jy, we find that the expected total number of sources is 56, while in the same range we detect 75 sources. This appears to confirm the agreement between the detected and expected point sources.

4.3. The SRT C-band sample of supernova remnants

With the previously compiled catalog of compact sources detected in our map, we can perform a correlation between SNRs and SNR candidates in the field of M 31. For this purpose, we used the Lee & Lee (2014) SNR and SNR candidate catalog, which includes 156 sources, obtained with Hα and [SII] images of M 31. Using a $145''$ search radius we cross-matched the SNRs and SNR candidates catalog with our sample of point sources. The choice of a search radius of $145''$ is motivated by the size of the FWHM$_{\mathrm{SRT}} = 2.9'$. We found then that source numbers 241, 359, 622, 626, and 645 have at least one corresponding source in the SNR catalog. In particular, for the SRT source number 645 we have four corresponding sources within $145''$, three corresponding sources for the SRT source number 622, and 2 for number 241. The other two SRT sources have only one corresponding source each. In Fig. 8 we show all the 156 SNRs and SNR candidates (white contours) and the sources that have a corresponding source within a radius of $145''$ (cyan circles).

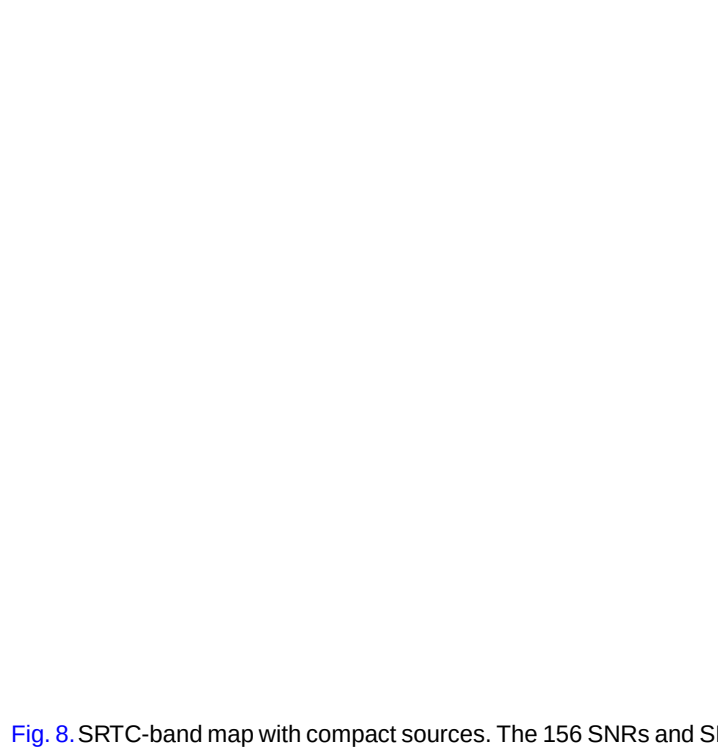

Fig. 8. SRT C-band map with compact sources. The 156 SNRs and SNR candidates from (Lee & Lee 2014) are overplotted with white contours. The SRT sources that have a corresponding source within a radius of 1:45′ are shown with cyan circles.

Table 3. SRT C-band sources with a correspondence in the Lee & Lee (2014) catalogue.

SRT source n.	Lee SNR n.	Distance (′)	6.6 GHz 1.4 GHz
241	50	0.87	0.42
359	17	0.93	0.49
622	156	0.96	0.16
626	144	0.78	0.31
645	97	0.09	0.01

In Table 3 we report the list of sources with a match in the Lee & Lee (2014) catalog, together with the ID in that same catalog, the distance from the center, and the spectral index between 1.4 and 6.6 GHz.

We note that the sources with a corresponding source in the SNR catalog are mostly characterized by a relatively flat spectrum. This is a bias most likely introduced by the achieved sensitivity at 6.6 GHz with SRT: if we assume two sources with the same 1 GHz amplitude, it is much more likely to detect the source with a flat spectrum than the source with a steeper one.

5. M 31 morphology

Studies of M 31 have revealed a normal disk galaxy with spiral arms wound up clockwise. The spiral arms are separated from each other by at least 4 kpc. The spiral pattern is somewhat distorted by the interactions of the galaxy with M 32 and M 110 (Gordon et al. 2006). The Spitzer Space Telescope (SST) revealed two spiral arms emerging from a central bar. The arms have a segmented structure and continue beyond the galaxy's ring mentioned above. The ring shape of M 31 was discovered

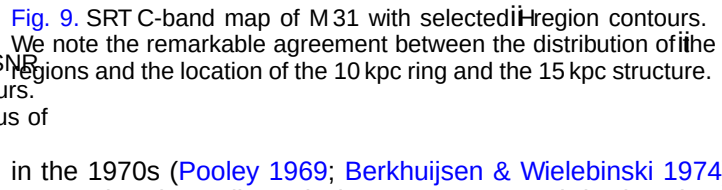

Fig. 9. SRT C-band map of M 31 with selected HII region contours. We note the remarkable agreement between the distribution of the HII regions and the location of the 10 kpc ring and the 15 kpc structure.

in the 1970s (Pooley 1969; Berkhuijsen & Wielebinski 1974). Comparing the radio emission at 6.6 GHz and the location of the 3691 HII regions presented in Azimlu et al. (2011) we find a strong correlation in the ring, as one can see in Fig. 9. The HII level contours denote 1, 3, or 6 HII regions inside each SRT C-band pixel, and so they are not flux density contours but are simply an indication of the positions of the HII regions.

The ring structure is believed to be the result of the interaction with M 32 over 200 million years ago. The M 32 galaxy likely passed through the disk of M 31, which left M 32 stripped of more than half of its mass (D'Souza & Bell 2018). The nucleus of M 31 is home to a dense, compact star cluster. A total of 35 black holes have been detected in M 31, of which 7 are within 0.3 kpc of its center (Barnard et al. 2013). These black holes formed by gravitational collapse of massive stars and have a mass of between approximately five and ten times that of the Sun.

Radio and microwave observations revealed emission from the central region and only from the external ring, while the central bar is not detected. The central bar, which is detected in all the IR images, is also not visible in the ancillary Effelsberg radio maps. As one can clearly see in Fig. 9, the 10 kpc ring and the 15 kpc structure, noted in IR maps (Haas et al. 1998; Gordon et al. 2006) are well correlated with the location of the HII regions in the SRT map. The 15 kpc structure is unfortunately at the edge of the Effelsberg maps, and in the following section, when these maps are used, it is not possible to disentangle thermal and nonthermal emission within these external regions.

The M 32 and NGC 205 galaxies, which fall inside the SRT coverage, are not detected because of their low radio emission. Brown et al. (2011) found that, at 1.4 GHz, M 32 and NGC 205 have respectively a flux density of 0.70 ± 0.05 mJy and 0.11 ± 0.05 mJy. Also, if a flat radio spectral index is assumed for these galaxies (most favorable scenario), their flux densities are compatible with the SRT confusion noise and therefore cannot be detected.

Fig. 10. Left panel: spectral index map extracted from 1.46 and 4.85 GHz Effelsberg maps and our SRT 6.6 GHz map. Right panel: spectral index noise map. The typical beam size (FWHM = 2.9′) is indicated with the black circle in the bottom-left corner of each panel.

In the following, we investigate the M 31 radio features by creating a spectral index map, and by studying the spectral index trend within the central region and the entire galaxy.

5.1. Spectral index map

We start by building a spectral index map across the whole M 31. In general, a flat spectral index is expected in regions whose emission is dominated by a thermal component, while a steeper spectrum is an indication of a substantial presence of nonthermal emission.

The spectral index value has been calculated on a pixel-by-pixel basis by taking into account only the pixels with flux densities greater than 3σ in all considered maps, where σ is the map sensitivity expressed in Jy beam^{-1}. Indeed, pixels below this threshold are those where the spectral index becomes very uncertain because of the presence of faint radio emission and radio noise. The spectral index map was created using Effelsberg maps at 1.46 GHz and 4.85 GHz and the SRT map at 6.6 GHz. We used the maps projected and then convolved to a $3'$ beam, as explained in Sect. 3.

The spectral index value and its 1σ uncertainty were computed pixel by pixel by fitting the relation:

$$f(\nu) = A \left(\frac{\nu}{1\,\mathrm{GHz}}\right)^{\alpha}, \quad (6)$$

where both A and α are free parameters. To perform the fitting, we used a Python implementation of Goodman and Weare's Markov chain Monte Carlo (MCMC) Ensemble sampler (Foreman-Mackey et al. 2013). The same MCMC was used in the following sections, to fit the emission in the central region and that in the ring, and to disentangle thermal and nonthermal emission maps. The spectral index map and its 1σ uncertainty are shown in Fig. 10.

Globally, the spectral index map shows values of $\alpha \simeq -0.7$ (light blue and light green pixels). In the northern and southern ring and in the central region, we can also find small patches (violet and blue pixels) not located at the edge of the map where the SRT and Effelsberg S/N is lower, with a spectral index around $\alpha = -0.4 \div -0.5$. These are the regions where thermal free-free emission is expected to be dominant and are likely to be H II regions, which are mainly located in these parts of the galaxy, as shown in Azimlu et al. (2011). In some inner and outer ring regions we find that the spectral index is larger than 0.9. This means that these regions are characterized mostly by synchrotron emission, with the steep slope indicating that an old population of electrons is responsible for the nonthermal emission.

Spectral index maps of M 31 have been built before (Berkhuijsen et al. 2003; Beck et al. 2020). We find excellent agreement between our spectral index map shown in Fig. 10 and the one extracted by Berkhuijsen et al. (2003), which is not surprising given the fact that, with the exception of the SRT C-band map, to extract the spectral index we used the same set of maps, at the same angular resolution. The spectral index values found by Beck et al. (2020) using Effelsberg maps at 1.465 and 8.350 GHz are generally smaller than ours by ~ 0.2. We can ascribe this discrepancy to the difference in total flux density between the SRT 6.6 GHz map and the new Effelsberg 8.35 GHz map. More specifically, the latter shows a flux density that is $\sim 15\%$ higher than the former. We identified some factors that could account for this discrepancy:

- The point sources in the two maps have been subtracted with different methods. Residual point sources in one map that have been removed from the other can affect the flux difference in both directions.
- Maps have been made with different telescopes, the data have been analyzed independently, and different software has been used.
- The total area covered by the two maps is different; this can affect the background estimate and the baseline subtraction. Moreover, Battistelli et al. (2019) showed that AME is the dominant emission mechanism in M 31 in the frequency range 10–60 GHz. This means that, at 8.35 GHz, AME must make up for 10–15% of the total integrated flux density, causing the spectral

Table 4. Spectral index values in the central region as a function of galactocentric distance.

Ring n.	Galactoc. distance (kpc)	Spectral index	S. index
1	0 0.34	0.62	0.14
2	0.34 1.02	0.63	0.10
3	1.02 1.70	0.68	0.09
4	1.70 2.38	0.77	0.09

trend to drift away from a simple power law. Therefore, AME can account for part of the difference between the two spectral index maps.

In the following sections, we explain how we used our spectral index map to choose regions in which to perform a detailed study of the decomposition between thermal and nonthermal emissions.

5.2. Spectral index trend

Hereafter, we evaluate the spectral index gradient across the galaxy and, in doing so, we separately analyze the properties of the central region. For this analysis we used the Effelsberg map at 2.7 GHz and all the other radio maps projected and convolved to $5'$ as explained in Sect. 3. We fitted a simple power law with two free parameters using the integrated flux densities in each given region instead of single pixel values, following the same procedure for the extraction of the spectral index map.

For the galaxy central region, we evaluated the spectral index within four concentric rings centered at (RA, Dec)= (10.70, 41.28) deg (see Table 4 for more details). For each ring, the total flux density was evaluated as:

$$F = S_{in} - S_{ext} \, \Omega_{in}; \quad (7)$$

where S_{in} is the brightness inside the integration region, S_{ext} is the background brightness and Ω_{in} is the solid angle subtended by the region. The thermal brightness uncertainty was computed as explained in Rubiæo-Martín et al. (2012) and then combined with the calibration error[9].

The spectral index as a function of distance from the galaxy center and the four rings where it was calculated are shown in Fig. 11. For each ring we used a position angle of 52 deg in the (RA, Dec) system and an eccentricity equal to 0.26. The spectral index within the central region is found to be approximately constant within the uncertainties. We further investigate the central region emission in Sect. 6.1 by decomposing thermal and nonthermal emission.

We also repeated the same analysis for the whole galaxy: in this case we used seven elliptical rings, centered at (RA, Dec)= (10.70, 41.28) deg, with the same position angle and eccentricity as those used for the central region. The details of the seven regions and the spectral index values are reported in Table 5.

The seven elliptical rings and the spectral index as a function of the distance from the galaxy center are shown in Fig. 12. The spectral index shows a clear positive gradient in the innermost 6 kpc (first three rings). In the outermost rings, the gradient changes sign twice, at 6 (decreasing) and at 10 kpc (increasing again), even though the values are compatible with a

[9] The calibration errors are considered to be 5% for all the maps.

Fig. 11. Upper panel: four elliptical rings used to compute the spectral index trend with the distance from the center of M 31. Lower panel: spectral index average radial profile calculated within the rings shown above.

Table 5. Spectral index values as a function of the galactocentric distance for the whole galaxy.

Ring n.	Galactoc. distance (kpc)	Spectral index	S. index
1	0 1.13	0.66	0.05
2	1.13 3.40	0.90	0.05
3	3.40 5.66	1.05	0.04
4	5.66 7.92	0.94	0.04
5	7.92 10.18	0.83	0.04
6	10.18 12.45	0.87	0.05
7	12.45 14.14	1.01	0.05

flat trend between 8 kpc and 12 kpc. Overall the 10 kpc ring presents smaller values with respect to the peak reached within the third ring. The average value of 0.9 found at distances greater than 4 kpc strongly hints at synchrotron emission being the predominant mechanism at these frequencies. The point at highest galactocentric distance corresponds to the edge of the ring: as expected, because of the aging of electrons, we found a

Fig. 16. Fit to the ux densities of the northern half of the 10 kpc ring (see Table 7). The t is characterized by χ^2_ν = 1:5. The error bars in the plot correspond to 2.

Fig. 17. Fit to the ux densities of the southern half of the 10 kpc ring (see Table 7). The t is characterized by χ^2_ν = 0:3. The error bars in the plot correspond to 2.

same ellipses as in Sect. 6.2. Data points and the t model are reported in Fig. 16. The t is characterized by a χ^2_ν = 1:5.

We note that in the upper ring the free-free emission at 1 GHz is only a fractional part of the total emission. Moreover, we have only a marginal detection for the free-free emission: the 1 GHz free-free amplitude is 1:5 , which is compatible with zero emission.

The thermal ux density, extrapolated to 6.6 GHz is about one-third of the synchrotron emission, while at 1 GHz it is 16 times weaker.

6.4. Southern ring region

We repeated here the analysis we carried out in Sect. 6.3, this time focusing on the southern half of the 10 kpc ring, the region delimitated by yellow dash-dotted lines in Fig. 13. Again, for this purpose, we used the same ellipses as in Sect. 6.2.

From an inspection of the spectral index map, we expect to nd a synchrotron spectral index which is higher than what we found for the northern region. Also, looking at the distribution of HII regions within the ring (Fig. 18), we expect a total thermal emission fraction at 6.6 GHz which is compatible with what we extracted for the northern ring. Figure 17 shows the best-t curve: the t model is characterized by χ^2_ν = 0:3.

As expected, the synchrotron spectral index value found for the southern region is steeper than the one we found for the northern region. However, due to the high uncertainties, the two synchrotron spectral indices turn out to be in agreement.

We note from the extrapolated ux densities at 6.6 GHz that within the southern ring the nonthermal emission is essentially twice the thermal emission. The integrated thermal emission on the two half ring regions is of the same order of magnitude, as predicted, while nonthermal emission was found to be higher in the northern half of the ring. The thermal emission fraction at 6.6 GHz in the southern half was found to be 38%, while in the northern half it makes up 26% of the total budget.

6.5. Thermal and nonthermal maps

As anticipated by the spectral index map, we found a typical synchrotron spectral index (0 0:8) in the central region, and a steeper spectrum with 0:8 for the 10 kpc ring. We can deduce from this that the galaxy presents sources of active electron injection in the central region, while the ring mainly hosts old electrons.

By using the free-free and synchrotron emission models in Eqs. (8) and (9) to reproduce the emission at the four different considered frequencies, we derived the thermal and the nonthermal contributions to the total ux density at a resolution of 5. We decided to leave the synchrotron and free-free emission amplitude at 1 GHz as free parameters, while the synchrotron spectral index has been xed to 1.06 in the ring and to 0.83 in the central region. Fixing the latter improves sensitivity on synchrotron and free-free amplitude values, removing the intrinsic degeneration between free-free and synchrotron emission models. Following this procedure, we were able to build spatially resolved emission maps for the thermal and nonthermal emission, which we present in Fig. 18.

The thermal map shown in the left panel of Fig. 18 shows a concentrated thermal emission in the southern and central part of the ring and diuse emission in the northern ring as expected given the distribution of HII regions (e.g., Azimlu et al. 2011). The regions of high thermal emission in the ring match the ones identi ed in previously published M 31 thermal maps (Berkhuijsen et al. 2003), and we generally nd good agreement in the whole ring and in the central region. Tabatabaei et al. (2013) separated free-free and synchrotron emission in M 31 using a template for the free-free emission from H emission line. Despite their dierent frequency, angular resolution, and decomposition technique, we noted good agreement in the location of the brightest thermal spots.

The value of the thermal peak emission in the ring is 19 mJy beam^{-1}, whereas the nonthermal intensity only reaches 10 mJy beam^{-1}. The thermal peak is located in the central part of the ring, (RA; Dec) = (11.17; 41.35) deg. In the southern ring, the thermal peak is 16 mJy beam^{-1}, while nonthermal emission is about one-third of that. High thermal emission is also found within the central region, in agreement with the results presented in Berkhuijsen et al. (2003). On the other hand, the H map extracted by Devereux et al. (1994) shows a bright bulge. These results seem to suggest that the M 31 bulge is also a star-forming region, despite no evidence of star formation in the central region being found by Ford et al. (2013). In the following section, we investigate the SFR in more detail, starting from the given thermal map. Globally, the average free-free noise values resulting from the pixel-by-pixel MCMC t were found to be in the range 0:5 2 mJy beam^{-1}. We stress the perfect agreement between our thermal map and the H map by Devereux et al. (1994) convolved to 5, see Fig. 19.